

Spatio-temporal variations of NO_y species in the northern latitudes stratosphere measured with the balloon-borne MIPAS instrument

A. Wiegele^{1,*}, A. Kleinert¹, H. Oelhaf¹, R. Ruhnke¹, G. Wetzel¹, F. Friedl-Vallon¹, A. Lengel^{1,**}, G. Maucher¹, H. Nordmeyer¹, and H. Fischer¹

¹Institut für Meteorologie und Klimaforschung, Forschungszentrum Karlsruhe, Karlsruhe, Germany

* now at: iMA Richter & Röckle, Freiburg, Germany

** now at: Carl Zeiss AG, Oberkochen, Germany

Received: 4 December 2007 – Published in Atmos. Chem. Phys. Discuss.: 5 March 2008

Revised: 1 October 2008 – Accepted: 19 January 2009 – Published: 16 February 2009

Abstract. This paper presents the spatio-temporal distribution of NO_y species at altitudes between 14 and 31 km as measured with the MIPAS-B instrument on the morning of 21 March 2003 in northern Scandinavia. At lower altitudes (below about 22 km), temperature variations, the distribution of ClONO_2 , and the tracer N_2O reveal the dynamics through the edge of the late arctic polar vortex. At higher altitudes, continuous measurement before, during, and after sunrise provides information about photochemistry illustrating the evolution of the photochemically active gases NO_2 and N_2O_5 around sunrise. The measured temporal evolution of NO_2 and N_2O_5 is compared to box modelling that is run along backward calculated trajectories. While the comparison of measured and modelled N_2O_5 reveals significant differences, there is a good agreement between the model and observations for NO_2 in terms of volume mixing ratios but the simulated decrease shortly after sunrise is underestimated compared to the measurements. The differences are attributed to the photolysis rates used in the box model calculations.

1 Introduction

Odd reactive nitrogen (NO_y) can be divided into reactive radicals NO_x and the less reactive reservoir species (Brasseur et al., 1999). For the following discussion, we define:

$$\text{NO}_x = \text{NO} + \text{NO}_2 + \text{NO}_3 \quad (1)$$



Correspondence to: A. Wiegele
(wiegele@ima-umwelt.de)

$$\text{NO}_y = \text{NO}_x + \text{HNO}_3 + 2 \cdot \text{N}_2\text{O}_5 + \text{ClONO}_2 + \text{HO}_2\text{NO}_2 \quad (2)$$

Nitrogen constituents, which are of minor importance for the NO_y budget, such as HNO_2 and BrONO_2 , are neglected here. The most important NO_y reactions are shown in Fig. 1 with $h\nu$ denoting photolytic dissociation reactions. The time constants for the photolytic reactions are quite different for the various species. Photolytic reactions of NO_2 and NO_3 are very fast (in the order of minutes), while photolysis of N_2O_5 is slower (in the order of several hours), and photolysis of HNO_3 and ClONO_2 is almost negligible in the lower stratosphere (Wayne, 2000) at high altitudes in winter.

Thus, the partitioning within NO_x is dominated by fast photochemistry. NO_2 is most prominent during nighttime, while a considerable amount of NO_x is converted to NO during daytime. The mixing ratios of NO and NO_3 differ between sunlit and dark conditions by a few orders of magnitude depending on altitude and latitude. In the middle and lower stratosphere, the reformation of NO_2 after sunset is about as fast as its photolytic dissociation after sunrise.

N_2O_5 is photolysed into NO_2 and NO_3 during the daytime. This reaction is much slower than the photolysis of NO_2 into NO , thus N_2O_5 is decreasing slowly during the whole daytime period. At nighttime, in the absence of sunlight, N_2O_5 is built up through the reaction of NO_2 with NO_3 leading to a slow increase of N_2O_5 during the nighttime with its maximum occurring around sunrise.

The NO_y family plays an important role in ozone chemistry, where the NO_y species have the ability to act in two ways. One is the ability to buffer reactive halogen species by forming reservoir gases and the other is its capability of catalytic ozone destruction (Brasseur et al., 1999). While the overall reactive nitrogen content NO_y is invariant at short timescales, the partitioning changes rapidly around sunset

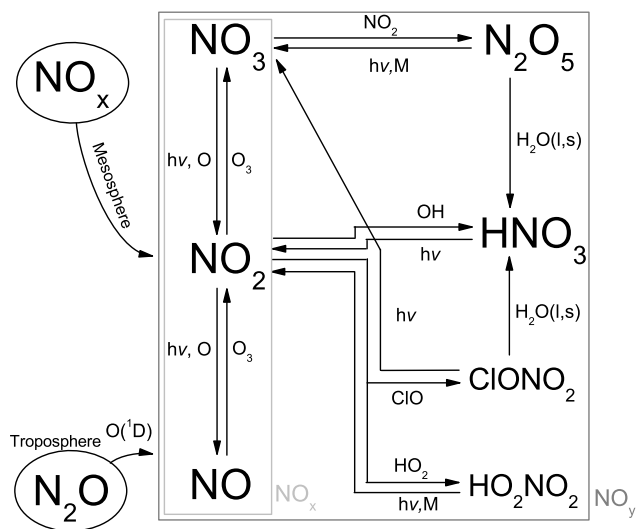


Fig. 1. Simplified reaction scheme of NO_y. All mentioned NO_y species except NO and NO₃ have been retrieved from MIPAS-B measurements for this study.

and sunrise and slowly during day- and nighttime. Furthermore, the amount of NO_y at a certain altitude differs between inside and outside the vortex.

Numerous measurements of individual species of the NO_y family have been reported over the last decades whereas observations of the complete partitioning and budget can be found less frequently in the literature. The latter have been mainly based on airborne and spaceborne remote sensing during day- and nighttime in emission or at sunrise and sunset in occultation (e.g. Toon, 1987; Abbas et al., 1991; Sen et al., 1998; Danilin et al., 1999; Osterman et al., 1999; Küll et al., 2002; Stowasser et al., 2002, 2003; Wetzel et al., 2002; Mengistu Tsidu et al., 2005).

From these various measurement techniques, diurnal variations of NO_y species can be best addressed by balloon-borne emission measurements. Emission instruments are capable of measuring in any azimuth direction at any time of the day, and a balloon platform allows sampling of the same air masses over several hours. Stowasser et al. (2003) have studied the variation of short-lived NO_y species around sunrise, but this was based on only three limb sequences, that have been performed one hour before, during, and three hours after sunrise.

For the study presented here, vertical profiles of the most important NO_y species have been measured quasi-continuously with high temporal resolution during several hours around sunrise. The measurements cover the altitude range from 14 to about 31 km and a spatial range of a few hundred km. This has allowed the study of both the temporal evolution of short-lived species and the distribution of longer-lived constituents across the vortex edge.

2 Measurement and sampling

The Michelson Interferometer for Passive Atmospheric Sounding, balloon-borne version, MIPAS-B, is a cryogenic Fourier transform spectrometer which measures the thermal emission of the atmosphere using the limb sounding geometry (Fischer and Oelhaf, 1996). Details about its layout, measurement technique, and data processing are reported by Friedl-Vallon et al. (2004) and references cited therein. The instrument covers the wavenumber region of 750 cm⁻¹ up to 2460 cm⁻¹ (equivalent to 4.06 μm up to 13.3 μm) where the most important NO_y species show prominent rotational-vibrational transitions.

The passive measurement of the thermal emission of atmospheric constituents allows MIPAS-B to measure at any time of the day and to point the line-of-sight (LOS) in elevation and azimuth according to the scientific needs. The remote sensing technique of MIPAS-B is suited for covering a range of altitudes in a short time interval and the azimuth angle can be adjusted relative to the position of the sun. These capabilities are essential for studying temporal evolutions at consistent illumination conditions.

2.1 Measurement technique and data analysis

The raw data measured by MIPAS-B are interferograms with a maximum optical path difference of 14.5 cm leading to a spectral resolution of about 0.07 cm⁻¹ (apodised). The sampling of one interferogram lasts about 10 s. The pointing system (Maucher, 1999) offers an accuracy of better than 150 m (3σ) with respect to tangent point altitudes.

The processing of the measured interferograms to calibrated spectra includes mathematical filtering, non-linearity correction, phase correction, and complex Fourier transformation (Kleinert, 2006; Kleinert and Trieschmann, 2007). The two point calibration that leads to radiance units is done by means of “deep space” (+20° elevation angle) and black body spectra. As a measure of the instrument sensitivity approximate Noise Equivalent Spectral Radiance (NESR) values for each spectral channel are compiled in Table 1.

For the temperature and trace gas retrievals the Karlsruhe Optimized and Precise Radiative transfer Algorithm KOPRA (Stiller et al., 2002) and the adapted inversion tool KOPRAFIT have been used. A Tikhonov-Phillips regularisation approach was applied which was constrained with respect to the form of an a priori profile. Spectroscopic data was taken from the spectroscopic database HITRAN01 (Rothman et al., 2003). Absorption cross-sections of ClONO₂ originate from Wagner and Birk (2003). The microwindows used for the retrieval are basically the ones described by Wetzel et al. (2002).

All retrievals have been performed with the same a priori information independent of the time of day. Error calculations include noise and LOS errors as well as spectroscopic errors for all retrievals. For the temperature retrieval,

Table 1. Spectral channels of MIPAS-B during the flight in March 2003 along with NESR values and prominent gases in these spectral regions.

Channel	Wavenumber region (cm ⁻¹)		approx. NESR (single spectrum) (nW/(cm ² sr cm ⁻¹))	Gases	
				NO _y	Further Species
1	750	1000	7	HNO ₃ , HO ₂ NO ₂ , ClONO ₂	CO ₂ , O ₃ , ClO, H ₂ O
2	1070	1557	4.5	N ₂ O ₅	CH ₄ , N ₂ O, O ₃ , H ₂ O
3	1557	1774	1.5	NO ₂	H ₂ O
4	1774	2460	1.8	NO	

uncertainties in CO₂ mixing ratios and gain errors are also taken into account. The gas retrievals then include the error caused by the resulting temperature errors.

Error contributions due to horizontal gradients along the line of sight can be regarded as minor for the reported observations because of the carefully defined measurement scenario and the well defined averaging kernels with narrow peaks of the contribution function around the tangent altitudes. For the retrieval of ClONO₂, for example, horizontal gradients of 1 ppbv per 100 km generate only small variations of up to 1% in the retrieved volume mixing ratios (vmrs).

The retrieval of NO profiles under consideration of non-local thermodynamic equilibrium (NLTE) effects has turned out to be extremely difficult for the balloon measurement geometry at this season and latitude, since both the stratospheric and the thermospheric contributions of NO were mainly located above the balloon altitude of about 31 km. Therefore, those two contributions could not be separated properly, leading to large errors in the retrieved profiles. Qualitatively, however, the raise of NO with sunrise is quite obvious. Because of the large uncertainties in the retrieved NO profiles, these results are not further discussed, and the NO_y budget calculations will be restricted to the nighttime measurements.

2.2 Sampling approach

In order to sample the temporal evolution of the NO_y species around sunrise, a dedicated measurement scenario has been performed covering the time from two hours before to three hours after sunrise. This scenario had to fulfil two requirements: First, the limb scans had to be comparably fast in order to get a high temporal resolution, and second, the direction of the measurement beam had to be chosen perpendicular to the azimuth direction of the sun in order to ensure symmetric illumination conditions along the LOS before and beyond the tangent point.

The first requirement was reached by averaging only two interferograms per tangent altitude (two have been chosen for the sake of redundancy). The tangent altitude sampling was 14 km, 17.5 km, 19.5 km, followed by equidistant steps of 1.5 km up to 30 km, 31 km, and completed by constant ele-

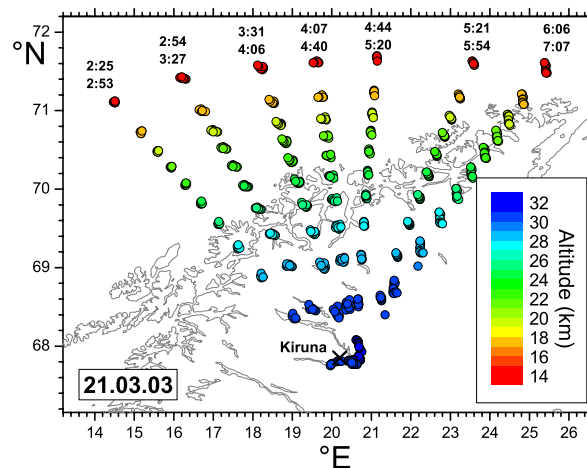


Fig. 2. Measurement scheme with its tangent points above northern Scandinavia. The colour code denotes the altitudes of the tangent points. For each azimuth direction, start and stop times of the measurements are indicated in UTC. The sunrise was between 03:40 UTC at the highest and 04:00 UTC at the lowest tangent points, during the measurements in the third azimuth direction from the west.

vations at -0.3° , 2° , and 20° . With this sampling scheme, the measurement duration of one limb profile was about 5 min. In total 58 limb sounding sequences have been recorded. In order to fulfil the second requirement the azimuth direction of the LOS was changed about every 30 min. Thus, individual limb sequences were grouped in 7 different azimuth angles.

The sampling of the measurements with the coordinates and altitudes of the tangent points is shown in Fig. 2. Very calm conditions at float altitude led to nearly no movement of the gondola during the recordings. It should be noted that this measurement pattern not only covers the temporal evolution of the NO_y species, but, by looking into different azimuth directions, also the spatial distribution within the covered range. While the temporal evolution is the dominant effect for short-lived species in the higher altitude range, variations of long-lived trace gases in the course of the measurements rather reflect the spatial distribution of the trace gases than their temporal evolution.

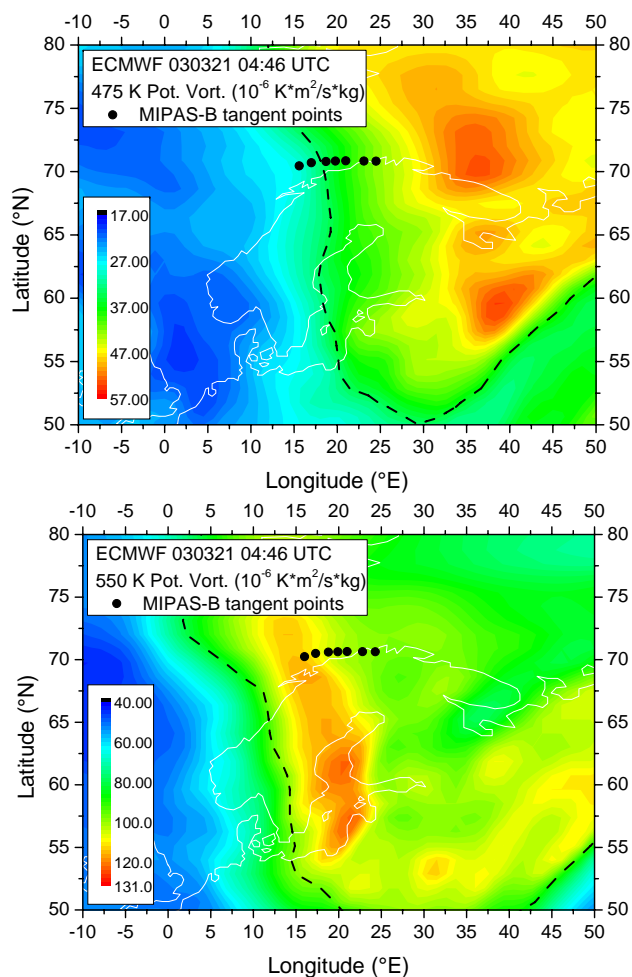


Fig. 3. Distribution of PV above north-eastern Europe on the morning of 21 March 2003. The upper panel shows the distribution at the potential temperature level 475 K (~ 19.5 km), the lower one at 550 K (~ 22.5 km). The tangent points of the respective altitudes are given as black dots. The dashed line shows the vortex edge according to Nash et al. (1996).

3 Meteorology

The early winter 2002/2003 was governed by low temperatures (Naujokat and Grunow, 2003) that were below the threshold temperature for the formation of polar stratospheric cloud (PSC) particles (Hanson and Mauersberger, 1988). After a major warming in mid-January followed by a reformation of the vortex, temperatures sank again below the threshold temperature for few days in early February. During those periods PSCs were observed (Spang et al., 2005) and denitrification had been measured by the MkIV instrument (Groß et al., 2005). Groß et al. (2005) have modelled the PSC formation as well as denitrification and give a more detailed view about the meteorological conditions during the winter 2002/2003.

The MIPAS-B measurements have been performed during a balloon flight above Kiruna (Sweden) at 20th/21st of March 2003. At this time of the year, a weak arctic vortex still existed and its center was shifted to Scandinavia and northern Russia.

The vortex axis was tilted in the vertical (see Fig. 3), therefore the different tangent altitudes (Fig. 2) were partly inside and partly outside of the vortex. The fields of potential vorticity (PV), as well as an analysis of the edge of the polar vortex calculated according to Nash et al. (1996), have shown that the westerly tangent points at 17 km and 19 km were situated outside the vortex, while the easterly tangent points were inside. All tangent points above 21 km were clearly inside the vortex. At the lowest level (14 km) the vortex was not well defined anymore.

Regarding the time of the year an exceptionally high tropopause was found in the westernmost measurement region above the North Sea and Norway in the ECMWF temperature profiles and the distributions of the PV. The temperature profile of a radiosonde launched from Kiruna the same day shows a first strong inversion, indicating the tropopause, as high as almost 13 km.

In summary, the measurements taken at altitudes between 17 km and 21 km covered the edge of the polar vortex with strong horizontal gradients while weaker gradients could be expected above these altitudes, where the scanned air masses were situated inside of the vortex. Therefore, both features can be explored, the edge of polar vortex with its strong horizontal gradients in the lowermost stratosphere as well as the diurnal evolution of the shorter lived species in the middle stratosphere.

4 Observations

The measurements reflect different air masses across the vortex edge (mainly at lower altitudes) as well as diurnal variations (mainly at higher altitudes). Therefore, the discussion focuses first on temperature and longer lived species to characterise the dynamical and thermal state of the observed air volumes. Thereafter, the diurnal evolution of photolytically active species such as NO₂ and N₂O₅ will be discussed.

The following plots show the retrieved profiles in colour code. The observations in the different azimuth directions are separated by black bars. The time of measurement is displayed on the X-axis. This axis is not perfectly linear because of calibration measurements during the change of azimuth angles. The approximate longitudes of the tangent points, valid for an altitude of 21 km, are denoted as white numbers. They serve as indicator for the position relative to the vortex edge. Furthermore, Figs. 10 and 11 include the sunrise for different altitudes as a white solid line.

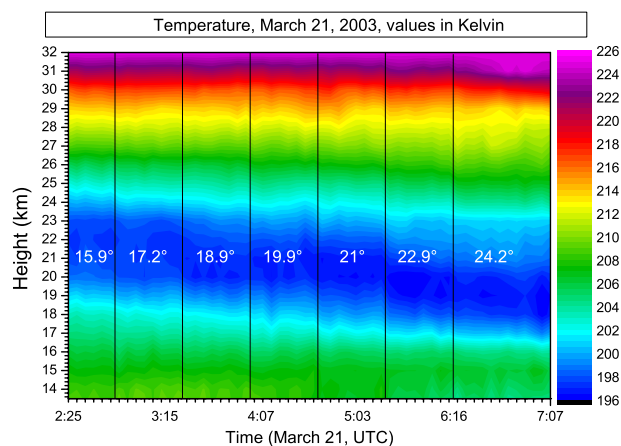


Fig. 4. Temperature across the edge of the polar vortex. The seven azimuth directions of the measurements are separated by black bars. The different blocks are labelled with the mean longitude of the tangent points at 21 km. The X-axis shows the time of the measurement.

4.1 Temperature

The retrieved temperature profiles are shown in Fig. 4. The temperature does not show mentionable diurnal variations, therefore the longitude, which serves as indicator for the position relative to the vortex edge, is more relevant than the time axis. Temperature errors of the individual profiles are in the order of 1 K (1σ , random and systematic error) and differences to ECMWF temperatures are in the range of 1 to 2 K (not shown).

The transection across the vortex edge shows differences between the air masses situated outside or inside the polar vortex. The more easterly the measurement is situated, the more the air masses are influenced by processes inside the vortex. The altitude of the minimum temperature decreases from about 22 km at the westernmost profiles to about 19 km at the easternmost profiles. In the altitude range of about 17 to 19 km, where the measurements cross the vortex edge, horizontal gradients are in the order of $1.5 \frac{\text{K}}{100\text{km}}$ with a maximum value of $1.8 \frac{\text{K}}{100\text{km}}$ at 18 km (see also Fig. 9).

4.2 N₂O

The retrieved N₂O profiles of all 58 measured sequences are collected in Fig. 5. The horizontal gradient of N₂O across the vortex edge in 18 km is shown in Fig. 9. Because of the longevity of N₂O, again the situation of the sampled air masses relative to the vortex is more important for the interpretation of the measurement than the time of day.

The dynamic tracer N₂O indicates the subsidence of air masses across the vortex edge very well. The subsidence is clearly visible below 21 km and is more pronounced at lower altitudes. From the 75 ppbv N₂O contour (cyan), a

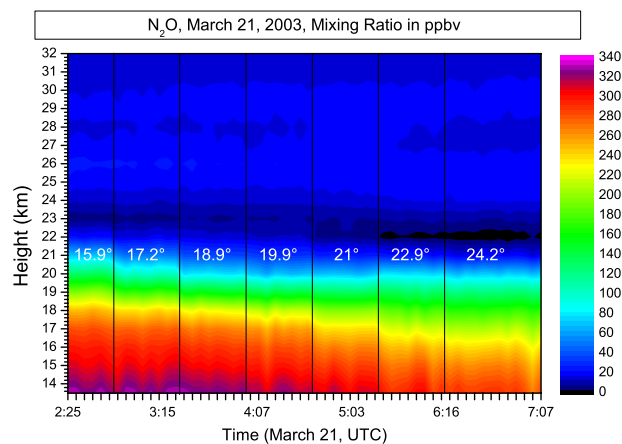


Fig. 5. Same as Fig. 4, but for N₂O.

subsidence of about 1 km can be derived (from 20.8 km to 19.8 km). Values of 225 ppbv (yellow) range from 18.5 km to 16 km, revealing a subsidence of about 2.5 km in this altitude range. It should be noted, however, that the actual subsidence may be larger than the values derived from these measurements because the measurements do not cover the whole range from well outside to well inside the vortex at all altitudes and mixing across the vortex edge may also have had an influence on the N₂O concentration (Müller et al., 2007). Above the cyan area, the relative subsidence is less obvious, because at higher altitudes the tangent points of different azimuth directions are relatively close together (see Fig. 2) and all situated inside the vortex. Furthermore, vertical gradients are very weak, which makes the quantification of any subsidence in that altitude region uncertain.

Very low mixing ratios of N₂O are measured at altitudes between about 22 and 24 km. Mixing ratios below 15 ppbv are marked in dark blue colours and the black area at this altitude in the two easternmost azimuth directions indicates extremely low N₂O concentrations close to zero. These mixing ratios can be attributed to air masses originating from the upper stratosphere as suggested by Müller et al. (2007). For a more detailed discussion of the dynamical situation of the late winter 2003 vortex, see also Engel et al. (2006).

The very high tropopause level mentioned in Section 3 is reflected by the high mixing ratios of N₂O at the lowest altitude of 14 km of the westernmost sequences. The maximum values of about 323 ppbv are in good agreement with the tropospheric mean value of 2003 (about 318 ppbv, WMO, 2006).

4.3 NO_y Partitioning

Vertical profiles of nighttime NO_y partitioning are shown in Fig. 6. The error bars include noise, temperature and LOS errors as well as spectroscopic errors (see also Sect. 2.1). The NO_y error bars are calculated as root of sum squares of the

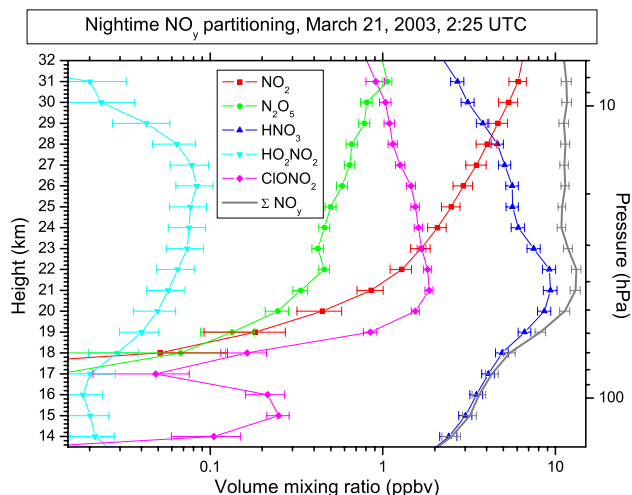


Fig. 6. Nighttime partitioning of NO_y except NO of the first measured sequence.

individual errors. HNO₃ dominates the budget up to 28 km altitude while higher up, the budget is dominated by NO₂. The nighttime contribution of NO to the total NO_y is negligible in the measurement range. Thus, the exclusion of NO is acceptable in the nighttime budget, while at daytime the NO contribution to total NO_y exceeds that of NO₂ at higher altitudes (not shown).

Several NO_y species measured with MIPAS-B during the same balloon flight but at different times and azimuth directions have been compared to coinciding satellite measurements (e.g. Höpfner et al., 2007; Wang et al., 2007; Wetzel et al., 2007, 2008), showing the overall high quality of data measured by MIPAS-B.

4.4 HNO₃

The retrieved mixing ratios of HNO₃ across the vortex edge are displayed in Fig. 7. In contrast to N₂O, HNO₃ cannot be regarded as good dynamical tracer as it undergoes photochemistry over weeks and may also be affected by denitrification, sedimentation, and renitrification.

From looking at the HNO₃ profiles, the subsidence of the air masses inside the vortex seems also visible but is much less obvious as compared to N₂O (see Fig. 5). Furthermore, the inside-outside contrast could underpin subsidence only for altitudes below about 19 km as it exhibits a different vertical behaviour than N₂O. Inside the vortex the HNO₃ peak mixing ratios are lower than outside by up to about 1 ppbv whereas, below the vmr peak, the HNO₃ abundance is increased. This pattern suggests some residual redistribution of HNO₃ after events of denitrification that were reported for periods earlier that winter (Groß et al. (2005), see also Sect. 3). However, the vertical redistribution of HNO₃ does not show up very clearly anymore at this time of the year

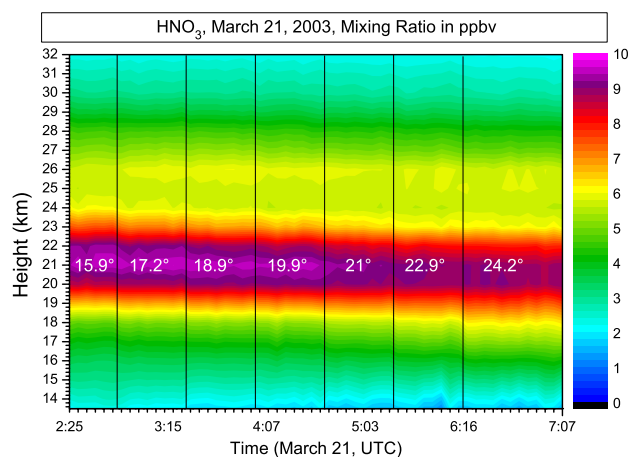


Fig. 7. Same as Fig. 4, but for HNO₃.

since after the major denitrification events that have taken place in January, dynamics and photochemistry might have washed out any more pronounced structures.

4.5 ClONO₂

As described in Sect. 3 the MIPAS-B measurements cover the vortex edge at lower altitudes. Figure 8 shows the distribution of ClONO₂ across the vortex edge. After periods of strong chlorine activation, a chlorine nitrate ring is formed near the vortex edge in spring due to the recombination of ClO with NO₂. An intersection through this ring is clearly visible in Figs. 8 and 9. Maximum ClONO₂ mixing ratios of up to 2.5 ppbv appear inside of the vortex close to the edge pointing back at previously strong chlorine activation.

The retrieved ClONO₂ profiles show significant differences between adjacent azimuth directions (separated by thin vertical lines), revealing the very strong horizontal gradients of ClONO₂ at the edge of the polar vortex. The different subsidence at adjacent longitudes is clearly visible in the lower altitude range.

4.6 NO₂

Figure 10 shows the evolution of the NO₂ mixing ratios before, during, and after sunrise. The plot is performed like the figures shown before, but here the time of measurement has to be noted and the white solid line in the third azimuth direction displays the time of sunrise for the different altitudes.

The plot shows mixing ratios of NO₂ up to 6.5 ppbv during nighttime at the highest altitudes. At daytime, the mixing ratios at these altitudes are reduced to about 2.5 ppbv. The reduction during sunrise is quite fast and shows the fast photolysis rates of NO₂. For example, at 31 km, the decrease from 5.4 ppbv at local sunrise to 2.3 ppbv takes place within 65 min (see also Fig. 12). The diurnal variations are visible down to about 22 km.

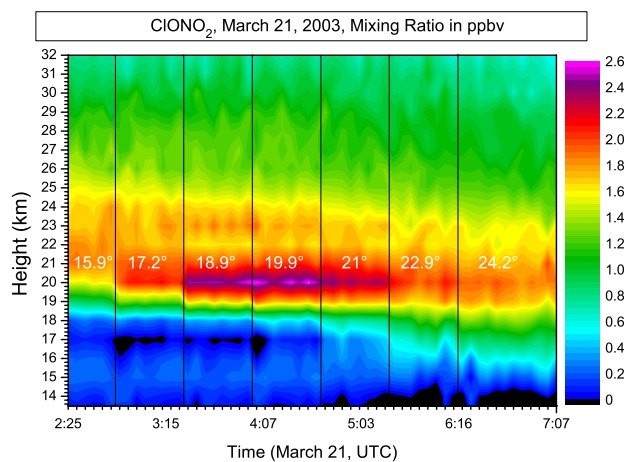


Fig. 8. Same as Fig. 4, but for ClONO₂.

4.7 N₂O₅

For the interpretation of the measured mixing ratios of N₂O₅ shown in Fig. 11 again the measurement time is more important than the longitude. This species is expected to reveal minimum mixing ratios around sunset and maximum mixing ratios around sunrise as described in Sect. 1.

Although the results of N₂O₅ are a little noisier than those of e.g. NO₂, the tendencies are obvious. As expected, the maximum of the mixing ratios is found around sunrise. The peak mixing ratio of 1.15 ppbv is measured at an altitude of 30 km few minutes after local sunrise (see also Fig. 12).

The mixing ratios at altitudes below 25 km do not show a significant response to changing sunlit conditions. The low volume mixing ratios of N₂O₅ at about 23 km in the easterly profiles can again be explained with the reduced NO_y content caused by the already mentioned downward transport from the upper stratosphere.

5 Modelling

A box model has been used to compare the MIPAS-B measurements with state-of-the-art chemistry modelling. For the model calculations, backward trajectories originating from the tangent points and times of the MIPAS-B measurements have been calculated.

5.1 Trajectories

The backward trajectory calculations (Langematz et al., 1987; Reimer and Kaupp, 1997) are based on the ECMWF analysis given every 6 h with a resolution of 2.5° in latitude and longitude. The trajectories are calculated on isentropic surfaces taking into account radiative heating and cooling with climatological heating rates.

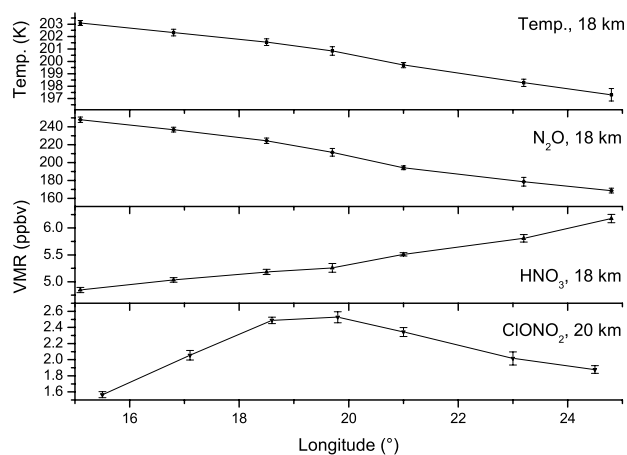


Fig. 9. Temperature and vmrs of N₂O, HNO₃ in 18 km, and ClONO₂ in 20 km altitude as a function of longitude. This plot reveals the gradients across the vortex edge in the respective altitudes. For each azimuth direction, the mean value of all measurement sequences is shown. The error bars denote the standard deviation (1 σ) of the results within one azimuth direction.

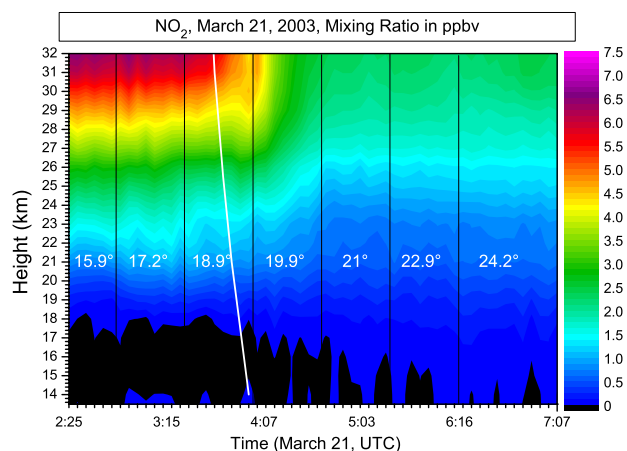


Fig. 10. Same as Fig. 4, but for NO₂. Here, the added white solid line denotes the time of the local sunrise, which is altitude dependent.

At each altitude, the box model was run for a duration of 3 days along the calculated backward trajectories, ending at the tangent points of the MIPAS-B measurements. In order to compare the model results to the measurements, the trajectories ending at the times and locations of measurements for the first (westernmost) azimuth direction have been extended along so-called synthetic trajectories which are defined by the times and locations of the following MIPAS-B measurements of the same altitude. These synthetic trajectories do not represent the transport of the air parcels anymore; they give only the model results along the MIPAS-B measurements.

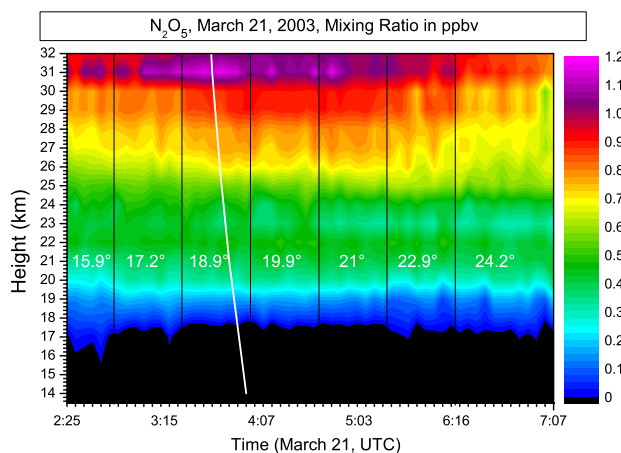


Fig. 11. Same as Fig. 10, but for N₂O₅.

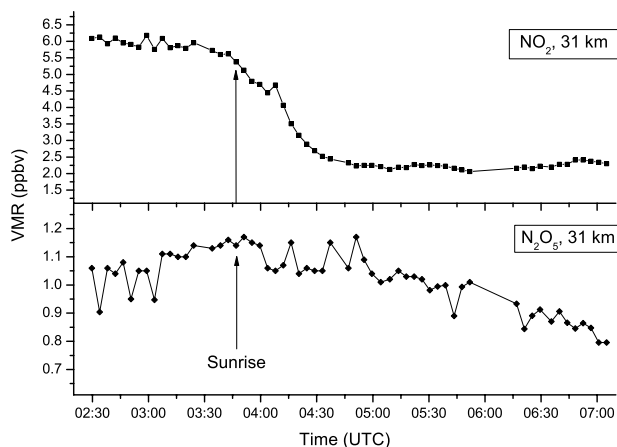


Fig. 12. vmrs of NO₂ and N₂O₅ in 31 km altitude as a function of time.

Furthermore, for each tangent altitude and azimuth direction of the measurements, individual trajectories have been determined and model calculations along these individual trajectories have been performed. The model results at the measurement points calculated with the individual trajectories do not differ significantly from the results calculated along the synthetic trajectories. Therefore, solely the results of the box modelling along the backward trajectories of the first azimuth direction in combination with the synthetic trajectories along the points of measurements will be discussed further.

5.2 Box model

The box model is a zero dimensional chemistry model described by Ruhnke and Röth (1995) and includes rate coefficients taken from Sander et al. (2003). The photolysis rates are precalculated for the different altitude levels of the trajec-

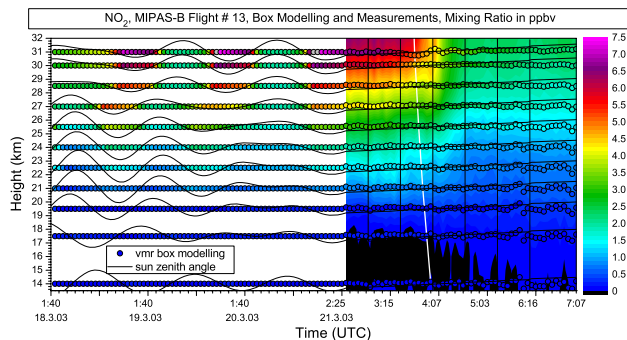


Fig. 13. Comparison between measured and modelled NO₂ mixing ratios. Model results are figured as coloured circles while the measurements results are plotted at the right hand side in the background. Again, the white line denotes the time of the local sunrise.

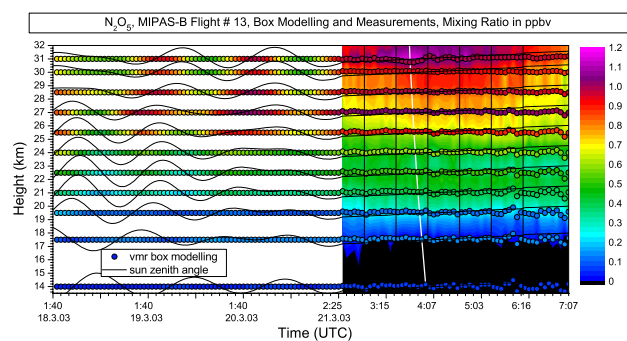


Fig. 14. Same as Fig. 13 but for N₂O₅.

tories with the radiation transfer model ART (Röth, 2002). Therein, the solar zenith angle dependence of the photolysis rates of each substance at a distinct altitude is given by the following parametrisation:

$$f = f_0 e^{b*[1-\sec(c\chi)]} \quad (3)$$

Therein f_0 is the photolysis rate at overhead sun conditions and the coefficients b and c describe the solar zenith angle dependency of the photolysis rate.

As the photolysis rates depend especially on the ozone profile, a climatological ozone profile, normalised to the mean ozone column measured by MIPAS-B, has been used to calculate the photolysis rates as realistically as possible. For the albedo, a constant value of 0.7 has been used. The box model takes into account 48 different gases, combined in nine families, and includes 167 reactions, of which 39 are photolytic. During the three days of backward trajectory calculations prior to the start of the measurements, time steps of the model are 10 min and the output is obtained every hour. During the time period of the measurements, each time step and output of the model is similar to the temporal resolution of the corresponding measurements (i.e. about 5 min).

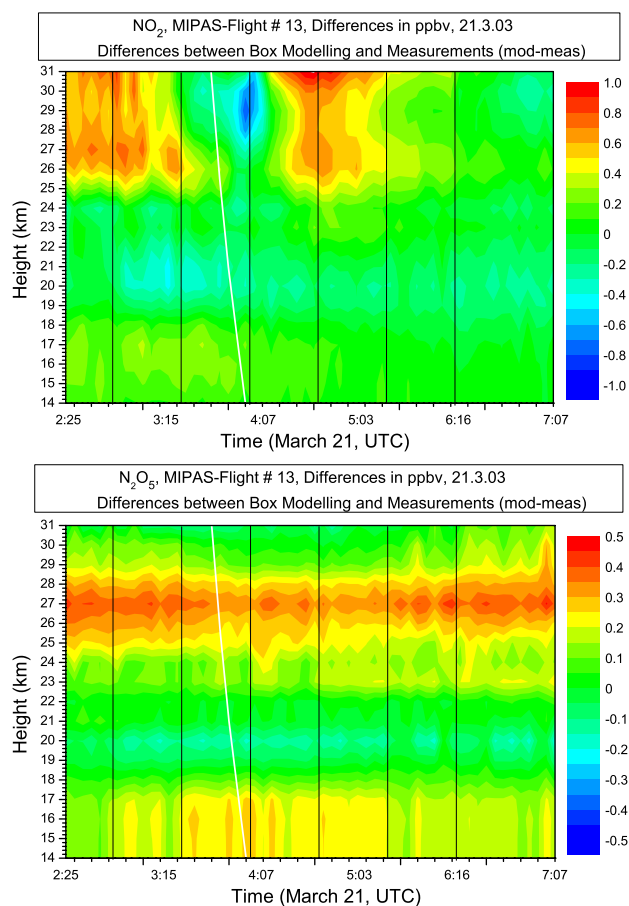


Fig. 15. Differences (model – measurement) for NO₂ (upper panel) and N₂O₅ (lower panel).

The zero dimensional modelling offers the possibility to simulate the chemistry of the measured air parcels for several days, because photochemistry is modelled according to the sunlit conditions along the trajectory. Pressure and temperature are taken from the trajectory calculation. This way of modelling is justified as long as horizontal and vertical mixing is negligible. For initialisation of the box model the mixing ratios of the gases used for the modelling are taken from a long-term simulation of the 3-D chemistry transport model KASIMA (Kouker et al., 1999), except for the constraints described below. A multi-annual KASIMA run with a grid of 5.6° in latitude and longitude is used with an interpolation to the starting coordinates of the trajectories. The initial NO_y was constrained to the total NO_y content measured by MIPAS-B. Therefore, the various NO_y species NO_{y,i} had to be normalised by the factor $\widehat{\text{NO}}_y$,

$$\widehat{\text{NO}}_y = \frac{\text{NO}_{y, \text{MIPAS-B}}}{\text{NO}_{y, \text{KASIMA}}}, \quad (4)$$

such that the NO_y partitioning given by KASIMA is preserved, but the total amount is constrained to the budget of

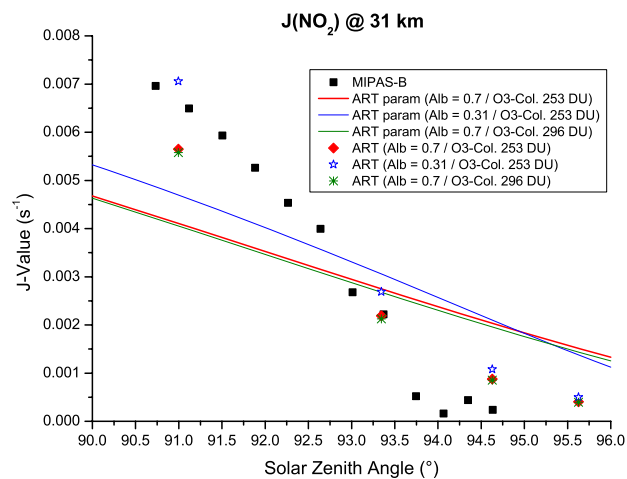


Fig. 16. Photolysis rates as a function of the solar zenith angle. Black squares: Values deduced from the measurements. Red line: Values from the model using the parametrisation as given in Eq. 3. Red squares: Exact values from the model. Furthermore, the model values for different O₃ columns and albedos are shown for the parametrisation (param) as well as for the exact values from the model.

the MIPAS-B measurements. The normalisation factor is in the order of 0.8 to 1.5. However, sensitivity studies performed with different initialisations (not shown) do not exhibit any non-linearity. With this normalisation the mixing ratios for the box modelling NO_{y,i,BOX} becomes:

$$\text{NO}_{y,i, \text{BOX}} = \widehat{\text{NO}}_y \cdot \text{NO}_{y,i, \text{KASIMA}} \quad (5)$$

These calculations have been done in terms of the definition of NO_y as given in Eq. (2).

The mixing ratios of the tracers N₂O, CH₄, as well as of ozone are also taken from the MIPAS-B measurement to avoid any biases in the initialisation fields modelled by KASIMA and to meet reality as good as possible.

5.3 Results of box modelling

Figures 13 and 14 present the time-resolved box modelling results together with the measurements for the photochemically active species NO₂ and N₂O₅, respectively. The time axis is extended to 3 days before the measurements to include the box model results for the simulated period. While this first part of the axis is linear, the time during measurement is stretched and not perfectly linear (see Sect. 4). The coloured circles overlaying the measurements denote the mixing ratios for the different altitudes in the same colour code as the measurements. Differences between model results and measurements thus appear as colour contrast between fore- and background. For clarity, the results of the box modelling during the 3 days before the measurement are displayed on fixed altitudes, although the air parcels experience some altitude excursion.

The thin black lines denote the local solar zenith angle in the respective altitudes. In this context, the fixed altitude denotes the horizon. Thus, when the black line is above the circles, the air parcel is sunlit, while during nighttime, the black line is below the circles. Depending on altitude and taking terrestrial refraction into account, sunrise and sunset occur at solar zenith angles of 93° to 95°.

5.3.1 NO₂ Model results

The modelling of NO₂ (Fig. 13) during the 3 days before the measurements shows the altitude-dependent behaviour of NO₂ with changing sunlit conditions very well. The mixing ratios are changing rapidly between night- and daytime according to the variation of the solar zenith angle. This is visible down to 19.5 km. Only few hours are necessary for the model to tune and no mentionable accumulation or consumption of NO_x due to an erroneous initialisation is visible during the modelled 3 days.

The comparison between the model and the measurement at the right side of the figure and in the upper panel of Fig. 15 shows that the daytime equilibrium mixing ratios are represented very well by the model. However, the nighttime mixing ratios above 25 km are too high in the model and some differences are evident during sunrise. In the model, the reduction of NO₂ starts earlier (before sunrise), such that the NO₂ vmr in the model even drops below the measured values (see Fig. 15). However, later on, in the fourth azimuth direction, the model provides significantly slower reductions of NO₂ than the measurement, such that the NO₂ vmr in the model again exceeds the NO₂ vmr in the measurement, and the equilibrium mixing ratio is obtained more than one hour later, pointing to slower photolysis in the model. This bias in time is less pronounced at lower altitudes.

5.3.2 N₂O₅ Model results

The diurnal variations of N₂O₅ (Fig. 14) during the first days of modelling show minor variations with time compared to those of NO₂ and well defined maxima at sunrise and minima at sunset above 21 km.

At the highest altitude, it appears that the N₂O₅ mixing ratio obtained by KASIMA, which is used for the model initialisation, is too low. Despite the weak accumulation of N₂O₅ during three days at the model run prior to the measurements, the comparison between the model and the measurements shows too small modelled volume mixing ratios at the highest altitude.

The most significant differences between the box model results and the observations occur at altitudes between 25.5 km and 28.5 km where the simulated N₂O₅ volume mixing ratios are larger than the measured ones (see also Fig. 15, lower panel). Beside initialisation problems due to an inappropriate partitioning of the individual NO_y species, differences in the temperatures along the trajectory could result

in a stronger simulated build up of N₂O₅ in particular during night time (Kircher et al., 1984). However, this explanation is not likely in our case, since the differences between retrieved MIPAS-B temperatures and ECMWF temperatures are mostly below 2 K. Such a difference would alter the N₂O₅ volume mixing ratio by only about 5%. As the main differences are obvious during night time, the assumed surface area density of sulphuric acid aerosols in the box model runs, which is kept constant during the 3 day simulation, is expected to be an important source of uncertainty for the modelled N₂O₅ evolution (Dufour et al., 2005).

6 Photolysis rates of NO₂

In order to get a better understanding of the discrepancies in the mixing ratios in the model and in the measurement around sunrise, photolysis rates for NO₂ ($J(\text{NO}_2)$) have been deduced from the measurements.

This requires some assumptions which are described in the following:

6.1 Assumptions

The basic relationship between NO and NO₂ is given by the following reactions:



The change in [NO₂] can be calculated from

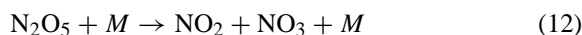
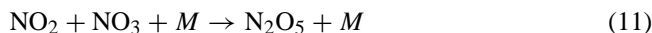
$$d[\text{NO}_2]/dt = k \times [\text{NO}] \times [\text{O}_3] - J(\text{NO}_2) \times [\text{NO}_2] \quad (9)$$

Equation 9 can be solved for $J(\text{NO}_2)$:

$$J(\text{NO}_2) = (k \times [\text{NO}] \times [\text{O}_3] - d[\text{NO}_2]/dt) / [\text{NO}_2] \quad (10)$$

In the steady state approximation $d[\text{NO}_2]/dt$ is set to zero, but at sunrise (and also sunset) the changes in solar flux are too rapid for this assumption (Gao et al., 2001).

In addition, NO₂ and NO₃ and thus NO_x (=NO+NO₂+NO₃) is in thermal equilibrium with N₂O₅:



Therefore, it can be assumed that an extended NO_x, which is defined as NO_{x,ext}=NO_x+2×N₂O₅, is constant during sunrise.

$$[\text{NO}_{x,\text{ext}}] = [\text{NO}_x] + 2 \times [\text{N}_2\text{O}_5] \quad (13)$$

6.2 Derivation of $J(\text{NO}_2)$ from MIPAS-B data

For the derivation of $J(\text{NO}_2)$ from MIPAS-B data, only the measurements in the third and the fourth azimuth direction (03:30 h–04:40 h) are considered as the largest differences in NO₂ occur shortly after sunrise (see Sect. 5.3.1).

As temperature, pressure, time, zenith angle, as well as the vmr of NO₂, N₂O₅, and O₃ at each tangent point are known from the MIPAS-B data, only NO has to be estimated to derive $J(\text{NO}_2)$ from MIPAS-B data. The first four limb sequences of the third azimuth direction (called S1 to S4) are performed during night time when [NO] is negligible and [NO_x]_{night} is set to the mean of [NO₂] of these four sequences:

$$[\text{NO}_x]_{\text{night}} = ([\text{NO}_2]_{\text{S1}} + [\text{NO}_2]_{\text{S2}} + [\text{NO}_2]_{\text{S3}} + [\text{NO}_2]_{\text{S4}}) / 4 \quad (14)$$

In addition, it is assumed that during the time period considered, [NO_{x,ext}] is constant. Thus, [NO_{x,ext}] can be determined similar to [NO_x]_{night}:

$$[\text{NO}_{x,\text{ext}}] = [\text{NO}_x]_{\text{night}} + ([\text{N}_2\text{O}_5]_{\text{S1}} + [\text{N}_2\text{O}_5]_{\text{S2}} + [\text{N}_2\text{O}_5]_{\text{S3}} + [\text{N}_2\text{O}_5]_{\text{S4}}) / 4 \quad (15)$$

With these assumptions, [NO] at a given time t can be calculated as:

$$[\text{NO}]_t = [\text{NO}_{x,\text{ext}}] - [\text{NO}_2]_t - 2 \times [\text{N}_2\text{O}_5]_t \quad (16)$$

When rewriting Eq. 10 as

$$J(\text{NO}_2)_t = (k \times [\text{NO}]_t \times [\text{O}_3]_t - ([\text{NO}_2]_t - [\text{NO}_2]_{t-1}) / \Delta t) / [\text{NO}_2]_t \quad (17)$$

we can calculate $J(\text{NO}_2)$ from MIPAS-B data:

$$J(\text{NO}_2)_t = (k \times ([\text{NO}_y] - [\text{NO}_2]_t - 2 \times [\text{N}_2\text{O}_5]_t) \times [\text{O}_3]_t - ([\text{NO}_2]_t - [\text{NO}_2]_{t-1}) / \Delta t) / [\text{NO}_2]_t \quad (18)$$

6.3 Results and discussion

The J values for NO₂ calculated according to Eq. 18 and the values used in the model (using Eq. 3) are displayed in Fig. 16 for an altitude of 31 km. While the photolysis rate in the model increases rather linearly with decreasing solar zenith angle (SZA), the photolysis rate deduced from the measurement is close to zero for SZAs above 93.5 degrees and increases linearly below. However, the slope is much steeper in the measured data, such that the J values at 91 degrees SZA exceed the values in the model by more than 50%. The lower J values used in the model explain the slower decrease of NO₂.

The discrepancy in the J values for NO₂ between the measurements and those used in the box model runs can be explained with the parametrisation of the J values in the model. The values of the parametrisation are based on a fit of the

originally calculated J values in the SZA range from 0° to 80° (E.-P. Röth, personal communication, 2008). Thus, the SZA range during sunrise which is analysed for $J(\text{NO}_2)$ in this paper is outside the fit interval of the parametrisation. This is obvious from Fig. 16 when comparing the $J(\text{NO}_2)$ values of the parametrisation to the originally calculated J values. These original J values are in much better agreement with the J values deduced from the MIPAS-B measurements. This leads to the conclusion that the parametrisation (Eq. 3) has its advantages mainly for global mean conditions with SZAs below 80° but for winter or spring arctic conditions at sunrise or sunset the fit procedure needs to be adjusted. An adjustment of the parametrisation for these conditions is currently in preparation (E.-P. Röth, personal communication, 2008).

The influence of the ozone column and the albedo on the model data has been investigated with additional sensitivity calculations using ART. The ozone column has been increased by about 43 DU up to 296 DU, which is at the upper range of the TOMS data around Kiruna at March 21, 2003, but these variations in the ozone column only have a marginal effect on the J values whereas they are rather sensitive to the albedo assumed. An albedo of 0.31 instead of 0.7, which has been applied for the box model runs, increases the J values significantly, bringing the model values closer to the measurement (see Fig. 16).

7 Conclusions

The results presented here show the ability of MIPAS-B to measure the diurnal variations of photochemically active NO_y species with high temporal resolution. Furthermore, the capability of measuring the spatial distribution of various trace gases across the vortex edge has been demonstrated. The measurements in March 2003 yield a cross section through the edge of the polar vortex as well as the temporal evolution of photochemically active NO_y species around sunrise. Spatial and temporal effects can be separated, because the measurements across the vortex edge have only occurred at lower altitudes (as can be seen from the PV distributions, Fig. 3), where photochemistry is less important. The measurements at the higher altitudes are situated well inside the vortex, so that chemistry can be investigated solely. The edge of the polar vortex and the relative subsidence of polar vortex air are well seen from the distribution of temperature and N₂O at a good spatial resolution. This spatial resolution allows to resolve the ring of enhanced ClONO₂ close to the vortex edge with its very strong horizontal gradients.

The measurements of species that are affected by photolysis clearly show the diurnal variation as expected for both NO₂ and N₂O₅.

The comparison with a box modelling along backward calculated trajectories reveals differences in particular shortly after sunrise. The modelled decrease of NO₂ after sunrise is

about three times slower than the decrease in the measurement. However, for SZAs above 93.5° the model already shows some photolysis which is not seen in the measurement (see Fig. 16) leading to a negative difference in the left panel of Fig. 15 for high altitudes shortly after sunrise.

One reason for the discrepancy between model and measurement is found in the parametrisation of the photolysis rates used in the box model. Especially in the high altitudes, the photolysis rates used in the model are significantly smaller than the photolysis rates that are deduced from the measurement. These differences are mainly caused by the *J* value parametrisation in the model which is based on a fit of the originally calculated *J* values in the SZA range from 0° to 80°. This parameterisation is clearly not appropriate for SZAs around 90° as they occur in our measurements. Furthermore, it has been shown that the assumptions on the albedo have a rather strong influence on the photolysis rate while errors in the overhead ozone profile only have a minor effect. The initialisation of the box model in particular with respect to the assumed chlorine activation is a further reason for the discrepancies between modelled and measured results.

Acknowledgements. The authors thank the CNES launching team for the excellent balloon operations, the ESRANGE team of SSC for logistical support, and the FU Berlin (B. Naujokat and K. Grunow) for meteorological support and trajectory calculations. Financial support by the DLR (Project 50EE0020) and ESA for the MIPAS-B balloon flights is gratefully acknowledged.

Edited by: P. Haynes

References

- Abbas, M. M., Kunde, V. G., Brasunas, J. C., Herman, J. R., and Massie, S. T.: Nighttime reactive nitrogen measurements from stratospheric infrared thermal emissions observations, *J. Geophys. Res.*, 96(D6), 10885–10897, 1991.
- Brasseur, G. P., Orlando, J. J., and Tyndall, G. S.: *Atmospheric Chemistry and Global Change*, Oxford University Press, 654 pp., 1999.
- Danilin, M. Y., Rodriguez, J. M., Hu, W., Ko, M. K. W., Weisenstein, D. K., Kumer, J. B., Mergenthaler, J. L., Russell, J. M., III, Koike, M., Yue, G. K., Jones, N. B., and Johnston, P. V.: Nitrogen species in the post-Pinatubo stratosphere: Model analysis utilizing UARS measurements, *J. Geophys. Res.*, 104(D7), 8247–8262, 1999.
- Dufour, G., Payan, S., Lefèvre, F., Eremenko, M., Butz, A., Jeseck, P., Té, Y., Pfeilsticker, K., and Camy-Peyret, C.: 4-D comparison method to study the NO_y partitioning in summer polar stratosphere - Influence of aerosol burden, *Atmos. Chem. Phys.*, 5, 916–926, 2005, <http://www.atmos-chem-phys.net/5/916/2005/>.
- Engel, A., Möbius, T., Haase, H. P., Bönisch, H., Wetter, T., Schmidt, U., Levin, I., Reddmann, T., Oelhaf, H., Wetzel, G., Grunow, K., Huret, N., and Pirre, M.: Observation of mesospheric air inside the arctic stratospheric polar vortex in early 2003, *Atmos. Chem. Phys.*, 6, 267–282, 2006, <http://www.atmos-chem-phys.net/6/267/2006/>.
- Fischer, H. and Oelhaf, H.: Remote sensing of vertical profiles of atmospheric trace constituents with MIPAS limb-emission spectrometers, *Appl. Optics*, 35, 2787–2796, 1996.
- Friedl-Vallon, F., Maucher, G., Seefeldner, M., Trieschmann, O., Kleinert, A., Lengel, A., Keim, C., Oelhaf, H., and Fischer, H.: Design and characterization of the balloon-borne Michelson Interferometer for Passive Atmospheric Sounding (MIPAS-B2), *Appl. Optics*, 43, 3335–3355, 2004.
- Gao, R. S., Del Negro, L. A., Swartz, W. H., Salawitch, R. J., Lloyd, S. A., Proffitt, M. H., Fahey, D. W., Donnelly, S. G., Neuman, J. A., Stimpfle, R. M., and Bui, T. P.: *J*(NO₂) at High Solar Zenith Angles in the Lower Stratosphere, *Geophys. Res. Lett.*, 28(12), 2405–2408, 2001.
- Groß, J.-U., Günther, G., Müller, R., Konopka, P., Bausch, S., Schlager, H., Voigt, C., Volk, C. M., and Toon, G. C.: Simulation of denitrification and ozone loss for the Arctic winter 2002/2003, *Atmos. Chem. Phys.*, 5, 1437–1448, 2005, <http://www.atmos-chem-phys.net/5/1437/2005/>.
- Hanson, D. R. and Mauersberger, K.: Laboratory studies of the nitric acid trihydrate: Implications for the south polar stratosphere, *Geophys. Res. Lett.*, 15, 855–858, 1988.
- Höpfner, M., von Clarmann, T., Fischer, H., Funke, B., Glatthor, N., Grabowski, U., Kellmann, S., Kiefer, M., Linden, A., Milz, M., Steck, T., Stiller, G. P., Bernath, P., Blom, C. E., Blumenstock, Th., Boone, C., Chance, K., Coffey, M. T., Friedl-Vallon, F., Griffith, D., Hannigan, J. W., Hase, F., Jones, N., Jucks, K. W., Keim, C., Kleinert, A., Kouker, W., Liu, G. Y., Mahieu, E., Mellqvist, J., Mikuteit, S., Notholt, J., Oelhaf, H., Piesch, C., Reddmann, T., Ruhnke, R., Schneider, M., Strandberg, A., Toon, G., Walker, K. A., Warneke, T., Wetzel, G., Wood, S., and Zander, R.: Validation of MIPAS ClONO₂ measurements, *Atmos. Chem. Phys.*, 7, 257–281, 2007, <http://www.atmos-chem-phys.net/7/257/2007/>.
- Kircher, C. C., Margitan, J. J., and Sander, S. P.: Pressure and temperature dependence of the reaction NO₂+NO₃+M yields N₂O₅+M, *J. Phys. Chem.*, 88(19), 4370–4375, 1984.
- Kleinert, A.: Correction of detector nonlinearity for the balloon-borne Michelson Interferometer for Passive Atmospheric Sounding, *Appl. Optics*, 45, 425–431, 2006.
- Kleinert, A. and Trieschmann, O.: Phase determination for a Fourier transform infrared spectrometer in emission mode, *Appl. Optics*, 46, 2307–2319, 2007.
- Kouker, W., Langbein, I., Reddmann, T., and Ruhnke, R.: The Karlsruhe Simulation Model of the Middle Atmosphere (KASIMA), Version 2, *Wissenschaftliche Berichte, FZKA 7278*, 60 pp., Forschungszentrum Karlsruhe, Germany, 1999.
- Küll, V., Riese, M., Tie, X., Wiemert, T., Eidmann, G., Offermann, D., and Brasseur, G. P.: NO_y partitioning and aerosol influences in the stratosphere, *J. Geophys. Res.*, 107(D23), 8183, doi:10.1029/2001JD001246, 2002.
- Langematz, U., Labitzke, K., and Reimer, E.: Synoptic analysis and trajectories during the MAP/GLOBUS campaign 1983. *Planetary and Space Science*, 35(5), 525–538, doi:10.1016/0032-0633(87)90120-6, 1987.
- Maucher, G.: Das Sternreferenzsystem von MIPAS-B2: Sichtlinien-Bestimmung für ein ballongetragenes Spektrometer zur Fernerkundung atmosphärischer Spurengase, *Rep. FZKA*

- 6227, Forschungszentrum Karlsruhe GmbH, Karlsruhe, Germany, 1999.
- Mengistu Tsidu, G., Stiller, G. P., von Clarmann, T., Funke, B., Höpfner, M., Fischer, H., Glatthor, N., Grabowski, U., Kellmann, S., Kiefer, M., Linden, A., Lopez-Puertas, M., Milz, M., Steck, T., and Wang, D.-Y.: NO_y from Michelson Interferometer for Passive Atmospheric Sounding on Environmental Satellite during the Southern Hemisphere polar vortex split in September/October 2002, *J. Geophys. Res.*, 110, D11301, doi:10.1029/2004JD005322, 2005.
- Müller, R., Tilmes, S., Groß, J.-U., Engel, A., Oelhaf, H., Wetzela, G., Huret, N., Pirre, M., Catoire, V., Toon, G., and Nakajima, H.: Impact of mesospheric intrusions on ozone-tracer relations in the stratospheric polar vortex, *J. Geophys. Res.*, 112, D23307, doi:10.1029/2006JD008315, 2007.
- Naujokat, B. and Grunow, K.: The stratospheric arctic winter 2002/03: Balloon flight planning by trajectory calculation, in: Proceedings of the 16th ESA Symposium on European Rocket and Balloon Programmes and Related Research, ESA SP-530, 421–425, St. Gallen, 2003.
- Nash, E. R., Newman, P. A., Rosenfield, J. E., and Schoeberl, M. R.: An objective determination of the polar vortex using Ertel's potential vorticity, *J. Geophys. Res.*, 101, 9471–9478, 1996.
- Osterman, G. B., Sen, B., Toon, G. C., Salawitch, R. J., Margitan, J. J., Blavier, J.-F., Fahey, D. W., and Gao, R. S.: Partitioning of NO_y species in the summer Arctic stratosphere, *Geophys. Res. Lett.*, 26, 8, 1157–1160, doi:10.1029/1999GL900166, 1999.
- Reimer, E. and Kaupp, H.: Source identification of odour compounds using trajectories, Interreg II research Project OMKAS, Proc. of ECO-INFORMA, 97, 6–9 October 1997, Eco-Infompress, Bayreuth, 572–577, 1997.
- Röth, E.-P.: Description of the Anisotropic Radiation Transfer Model ART to Determine Photodissociation Coefficients, *Berichte des Forschungszentrums Jülich*, 3960, 2002.
- Rothman, L. S., Barbe, A., Benner, D. C., et al.: The HITRAN molecular spectroscopic database: edition of 2000 including updates through 2001, *J. Quant. Spectrosc. Ra.*, 82, 5–44, 2003.
- Ruhnke, R. and Röth, E.-P.: Ein Box-Trajektorien-Modell zur Analyse atmosphärischer Reaktionssysteme, *Berichte des Forschungszentrums Jülich* 3131, Forschungszentrums Jülich GmbH, ISSN 0944-2952, 1995.
- Sander, S. P., Friedl, R. R., Ravishankara, A. R., Golden, D. M., Kolb, C. E., Kurylo, M. J., Huie, R. E., Orkin, V. L., Molina, M. J., Moortgat, G. K., Finlayson-Pitts, B. J.: Chemical Kinetics and Photochemical Data for Use in Atmospheric Studies/Evaluation Number 14, JPL Publication 02-25, http://jpldataeval.jpl.nasa.gov/pdf/JPL_02-25_rev02.pdf, 2003.
- Sen, B., Toon, G. C., Osterman, G. B., Blavier, J.-F., Margitan, J. J., Salawitch, R. J., and Yue, G. K.: Measurements of reactive nitrogen in the stratosphere, *J. Geophys. Res.*, 103(D3), 3571–3586, 1998.
- Spang, R., Remedios, J. J., Kramer, L. J., Poole, L. R., Fromm, M. D., Müller, M., Baumgarten, G., and Konopka, P.: Polar stratospheric cloud observations by MIPAS on ENVISAT: Detection method, validation and analysis of the Northern Hemisphere winter 2002/2003, *Atmos. Chem. Phys.*, 5, 679–692, 2005, <http://www.atmos-chem-phys.net/5/679/2005/>.
- Stiller, G. P., von Clarmann, T., Funke, B., Glatthor, N., Hase, F., Höpfner, M., and Linden, A.: Sensitivity of trace gas abundances retrievals from infrared limb emission spectra to simplifying approximations in radiative transfer modelling, *J. Quant. Spectrosc. Ra.*, 72, 249–280, 2002.
- Stowasser, M., Oelhaf, H., Ruhnke, R., Wetzela, G., Friedl-Vallon, F., Kleinert, A., Kouker, W., Lengel, A., Maucher, G., Nordmeyer, H., Reddmann, Th., Trieschmann, O., von Clarmann, T., Fischer, H., and Chipperfield, M. P.: A characterization of the warm 1999 Arctic winter by observations and modeling: NO_y partitioning and dynamics, *J. Geophys. Res.*, 107(D19), 4376, doi:10.1029/2001JD001217, 2002.
- Stowasser, M., Oelhaf, H., Ruhnke, R., Kleinert, A., Wetzela, G., Friedl-Vallon, F., Kouker, W., Lengel, A., Maucher, G., Nordmeyer, H., Reddmann, T., and Fischer, H.: The variation of short-lived NO_y species around sunrise at mid-latitudes as measured by MIPAS-B and calculated by KASIMA, *Geophys. Res. Lett.*, 30(8), 1432, doi:10.1029/2002GL016727, 2003.
- Toon, G. C.: Detection of stratospheric nitrogen species, *Nature*, 330, p. 427, 1987.
- Wagner, G. and Birk, M.: New infrared spectroscopic database for chlorine nitrate, *J. Quant. Spectrosc. Ra.*, 82, 443–460, 2003.
- Wang, D. Y., Höpfner, Mengistu Tsidu, G., Stiller, G. P., von Clarmann, T., Fischer, H., Blumenstock, T., Glatthor, N., Grabowski, U., Hase, F., Kellmann, S., Linden, A., Milz, M., Oelhaf, H., Schneider, M., Steck, T., Wetzela, G., López-Puertas, M., Funke, B., Koukouli, M. E., Nakajima, H., Sugita, T., Irie, H., Urban, J., Murtagh, D., Santee, M. L., Toon, G., Gunson, M. R., Irion, F. W., Boone, C. D., Walker, K., and Bernath, P. F.: Validation of nitric acid retrieved by the IMK-IAA processor from MIPAS/ENVISAT measurements, *Atmos. Chem. Phys.*, 7, 721–738, 2007, <http://www.atmos-chem-phys.net/7/721/2007/>.
- Wayne, R. P.: Chemistry of atmospheres: an introduction to the chemistry of the atmospheres of earth, the planets and their satellites, Oxford Univ. Press, 806 pp., 2000.
- Wetzela, G., Oelhaf, H., Ruhnke, R., Friedl-Vallon, F., Kleinert, A., Kouker, W., Maucher, G., Reddmann, T., Seefeldner, M., Stowasser, M., Trieschmann, O., von Clarmann, T., Fischer, H.: NO_y partitioning and budget and its correlation with N₂O in the Arctic vortex and in summer midlatitudes in 1997, *J. Geophys. Res.*, 107(D16), 4280, doi:10.1029/2001JD000916, 2002.
- Wetzela, G., Bracher, A., Funke, B., Goutail, F., Hendrick, F., Lambert, J.-C., Mikuteit, S., Piccolo, C., Pirre, M., Bazureau, A., Bellotti, C., Blumenstock, T., De Mazière, M., Fischer, H., Huret, N., Ionov, D., López-Puertas, M., Maucher, G., Oelhaf, H., Pommereau, J.-P., Ruhnke, R., Sinnhuber, M., Stiller, G., Van Roozendaal, M., and Zhang, G.: Validation of MIPAS-ENVISAT NO₂ operational data, *Atmos. Chem. Phys.*, 7, 3261–3284, 2007, <http://www.atmos-chem-phys.net/7/3261/2007/>.
- Wetzela, G., Sugita, T., Nakajima, H., Tanaka, T., Yokota, T., Friedl-Vallon, F., Kleinert, A., Maucher, G., and Oelhaf, H.: Technical Note: Intercomparison of ILAS-II version 2 and 1.4 trace species with MIPAS-B measurements, *Atmos. Chem. Phys.*, 8, 1119–1126, 2008, <http://www.atmos-chem-phys.net/8/1119/2008/>.
- WMO: Greenhouse Gas Bulletin, 4 pp., <http://www.wmo.ch/pages/prog/arep/gaw/ghg/documents/ghg-bulletin-en-11-06.pdf>, 2006.